

Nonlinear dynamics and energy transfer for two rotating dipoles in an external field: A three-dimensional analysis

Rosario González-Férez,¹ Manuel Iñarrea,² J. Pablo Salas,² and Peter Schmelcher^{3,4}

¹*Instituto Carlos I de Física Teórica y Computacional,
and Departamento de Física Atómica, Molecular y Nuclear,
Universidad de Granada, 18071 Granada, Spain*

²*Área de Física, Universidad de La Rioja, 26006 Logroño, La Rioja, Spain*

³*The Hamburg Center for Ultrafast Imaging,
Luruper Chaussee 149, 22761 Hamburg, Germany*

⁴*Zentrum für Optische Quantentechnologien, Universität Hamburg,
Luruper Chaussee 149, 22761 Hamburg, Germany*

(Dated: August 23, 2021)

Abstract

We investigate the structure and the nonlinear dynamics of two rigid polar rotors coupled through the dipole-dipole interaction in an external homogeneous electric field. In the field-free stable head-tail configuration, an excess energy is provided to one of the dipoles, and we explore the resulting three-dimensional classical dynamics. This dynamics is characterized in terms of the kinetic energy transfer between the dipoles, their orientation along the electric field, as well as their chaotic behavior. The field-free energy transfer mechanism shows an abrupt transition between equipartition and non-equipartition regimes, which is independent of the initial direction of rotation due to the existence of an infinite set of equivalent manifolds. The field-dressed dynamics is highly complex and strongly depends on the electric field strength and on the initial conditions. In the strong field regime, the energy equipartition and chaotic behavior dominate the dynamics.

PACS numbers: **05.45.-a 05.60.Cd 37.10.Vz**

I. INTRODUCTION

The experimental availability of ultracold dipolar gases represents a strong motivation for the investigation of the physical phenomena related to the long-range and anisotropic dipole-dipole interaction [1]. By tuning the dipole-dipole interaction, the dipolar gas properties can be significantly modified giving rise to a rich variety of novel applications, such as, the creation of novel quantum liquids [2–4], exotic spin dynamics [5, 6], and the control of ultracold chemical reactions [7–9], thermalization [10] or energy exchange [11–14].

The mechanism of energy transport mediated by the dipole-dipole interaction is closely related to the nonlinear behavior of many-body systems and has attracted special attention in classical dynamics [15–20]. Most of the nonlinear dynamical studies on coupled rotating dipoles restrict their motion to planar rotations. As a consequence, each dipole is described by one angle and the number of degrees of freedom of the system is equal to the number of dipoles. A natural extension of these studies is to allow the dipoles to perform three-dimensional (3D) overall rotations, and, to the best of our knowledge, the corresponding literature is very scarce. The 3D classical dynamics has been explored for isolated rotors, such as diatomic or symmetric top molecules, exposed to combinations of external electric fields [21, 22]

In our previous work [18], we studied the classical dynamics of two polar rotors, coupled by the dipole-dipole interaction, in the presence of an external electric field in a planar invariant manifold. By restricting the motion of the dipoles to the invariant manifold, the system has two degrees of freedom. The energy transfer mechanism between the dipoles for varying field strength has been analyzed in terms of the phase space structure of the system. Here, we extend this previous study by exploring the complete 3D classical dynamics allowing the dipoles to rotate in any direction in space. Since the rotors motion is not restricted to a planar manifold as in Ref. [18], each dipole is described by two angles, and we encounter a Hamiltonian system with four degrees of freedom. We assume that the dipoles are initially in the stable head-tail configuration with fixed spatial positions. This stable configuration is perturbed by adding a certain excess energy to one of the dipoles, which starts rotating from the head-tail configuration axis, while at the same time the electric field is turned on. The follow up dynamics is investigated in terms of the energy exchange mechanism and the orientations of the rotors induced by the electric field. We also explore the chaoticity of the

system by using a fast chaos indicator.

Due to the existence of the infinite set of equivalent manifolds, our field-free results show that the energy transfer mechanism is independent of the direction for which the dipole starts to rotate, which is in complete agreement with our previous results [18]. The field-dressed dynamics is highly complex and strongly depends on the strengths of the dipole and the electric field interactions as well as on the initial conditions. In the very weak field regime, when the dipole interaction is dominant, the energy transfer mechanism resembles the field-free case, although the border between the non-equipartition and equipartition regimes becomes more diffuse. As the electric field increases, the energy equipartition regime dominates the dynamics, although we still encounter regions of non-equipartition energy for certain initial conditions. For strong fields, the two dipoles are significantly oriented along the electric field axis. When the electric field is turned on, the system becomes non-integrable so that there appears chaotic motion. For low and intermediate values of the field, the degree of chaoticity increases as the interaction with the electric field becomes more dominant. Surprisingly, for strong electric fields the chaoticity of the system remains very pronounced which is quite unexpected because the gradual increase of the field would eventually lead the system to its integrable limit. Indeed, we verified that, for very large values of the electric field, a slow crossover to an integrable phase space takes place.

This work is organized as follows. In Sec. II we discuss the classical Hamiltonian of the system, its symmetries and invariant manifolds. The underlying equilibrium points are also presented. In Sec. III we explore the time evolution of the energy transport between the dipoles and their orientations with varying initial conditions and for several the electric field strengths. The chaoticity of this systems is discussed in Sec. IV. Our conclusions are provided in Sec. V. In the Appendix, an exhaustive analysis of the existence, stability and bifurcations of the equilibria is given.

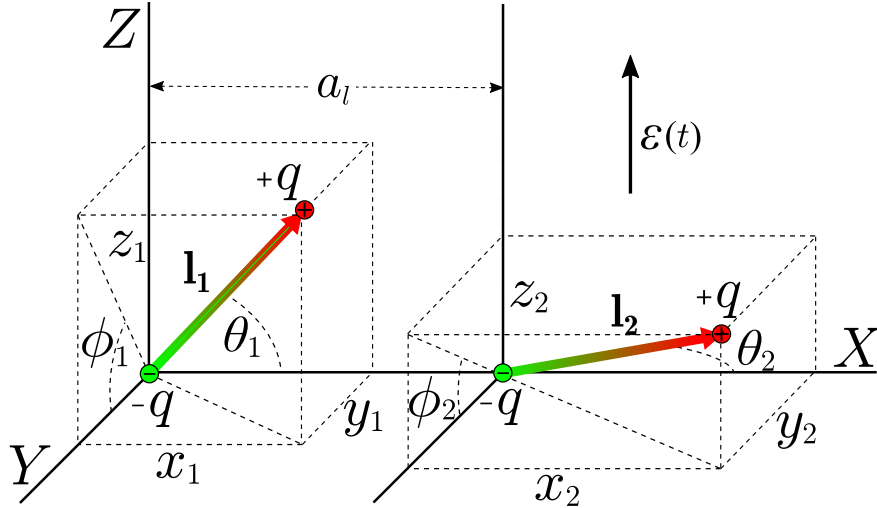


FIG. 1. Schematic representation of the two interacting dipoles

II. CLASSICAL HAMILTONIAN, SYMMETRIES AND INVARIANT MANIFOLDS

A. Classical Hamiltonian

The potential energy V_d between two dipoles with dipole moments \mathbf{d}_1 and \mathbf{d}_2 due to the mutual dipole-dipole interaction (DDI) is given by [23]

$$V_d = \frac{1}{4\pi\epsilon_0} \frac{(\mathbf{d}_1 \cdot \mathbf{d}_2) r^2 - 3(\mathbf{d}_1 \cdot \mathbf{r})(\mathbf{d}_2 \cdot \mathbf{r})}{r^5}, \quad (1)$$

with \mathbf{r} being their relative position. In our case, we consider two identical rigid rotors having electric dipole moments $\mathbf{d}_1 = q \mathbf{l}_1$ and $\mathbf{d}_2 = q \mathbf{l}_2$, with $d = |\mathbf{d}_1| = |\mathbf{d}_2| = q l$, being q and l the charge and length of the dipoles. Besides the DDI, the dipoles are in the presence of an external homogeneous time-dependent electric field $\mathcal{E}(t)$ parallel to the Laboratory Fixed Frame (LFF XYZ) Z -axis. Assuming that the positions of the rotors are fixed along the LFF X -axis and separated by a constant distance a_l (see Fig.1), the total interaction potential reads as follows

$$V(\mathbf{l}_1, \mathbf{l}_2, t) = -q \mathcal{E}(t)(z_1 + z_2) + \frac{q^2}{4\pi\epsilon_0 a_l^3} [\mathbf{l}_1 \cdot \mathbf{l}_2 - 3x_1 x_2], \quad (2)$$

where the vectors $\{\mathbf{l}_i = (x_i, y_i, z_i) \mid |\mathbf{l}_i| = l, i = 1, 2\}$ determine the orientation of the dipoles. The first term in (2) stands for the interaction with the external field and the second one for the DDI. Here, we assume that the homogeneous electric field has a turn-on

modeled by a linear ramp $f(t)$, so that $\mathcal{E}(t) = E_s f(t)$ with $f(t)$

$$f(t) = \begin{cases} \frac{t}{t_1} & \text{if } 0 \leq t < t_1 \\ 1 & \text{if } t \geq t_1 \end{cases} \quad (3)$$

This linear ramp was used in Ref. [24] and it also mimics the turn-on of laser pulses [25, 26].

If μ is the reduced mass of the dipoles, the dynamics of the system is governed by the classical Hamiltonian (the energy E)

$$E \equiv H = \sum_{i=1}^2 \frac{1}{2\mu} \left[P_{x_i}^2 + P_{y_i}^2 + P_{z_i}^2 \right] + V(\mathbf{l}_1, \mathbf{l}_2, t), \quad (4)$$

subject to the holonomic constraints $\{\mathbf{l}_i = (x_i, y_i, z_i) \mid |\mathbf{l}_i| = l, i = 1, 2\}$. At this point, and without loss of generality, we use a dimensionless version of the Hamiltonian (4) by expressing the energy in units of the parameter $\chi = d^2/4\pi\epsilon_0 a_l^3$ that controls the DDI. To do that, we introduce the dimensionless coordinates

$$\mathbf{l}'_i = (x'_i, y'_i, z'_i) = (x_i/l, y_i/l, z_i/l), \quad i = 1, 2,$$

and the dimensionless time $t' = t/t_d$, where $t_d = \sqrt{I/\chi}$ is the new unit of time being $I = \mu l^2$ the moment of inertia of the dipoles. After applying these transformations to (4), we arrive at the following dimensionless Hamiltonian

$$E' \equiv H' = \frac{H}{\chi} = \sum_{i=1}^2 \frac{1}{2} \left[P_{x_i}^{\prime 2} + P_{y_i}^{\prime 2} + P_{z_i}^{\prime 2} \right] + \mathcal{V}_1(\mathbf{l}'_1, \mathbf{l}'_2, t'). \quad (5)$$

where the potential $\mathcal{V}_1(\mathbf{l}'_1, \mathbf{l}'_2, t')$ reads as

$$\mathcal{V}_1(\mathbf{l}'_1, \mathbf{l}'_2, t') = -\beta f(t')(z'_1 + z'_2) + (\mathbf{l}'_1 \cdot \mathbf{l}'_2 - 3x'_1 x'_2). \quad (6)$$

In this way, the dynamics depends on the energy $E' \equiv H' = H/\chi$ and on the new (dimensionless) electric field parameter $\beta = dE_s/\chi$, which is the ratio between the strengths of the electric and the dipole-dipole interactions. For the sake of simplicity, we omit in the following the primes in Hamiltonian (5)

The aforementioned holonomic constraints between the Cartesian coordinates of the dipoles reduce the number of degrees of freedom from $6+1/2$ to $4+1/2$. By taking the LFF X -axis as the polar axis, the transformation between the Cartesian and the Euler angles $(\theta_1, \phi_1, \theta_2, \phi_2)$ of each rotor reads (see Fig.1)

$$x_i = \cos \theta_i, \quad y_i = \sin \theta_i \cos \phi_i, \quad z_i = \sin \theta_i \sin \phi_i, \quad i = 1, 2$$

and the Hamiltonian (5) converts to

$$H = \sum_{i=1}^2 \frac{1}{2} \left[P_{\theta_i}^2 + \frac{P_{\phi_i}^2}{\sin^2 \theta_i} \right] + \mathcal{V}_2(\theta_1, \phi_1, \theta_2, \phi_2; t), \quad (7)$$

where the interaction potential (2) is

$$\begin{aligned} \mathcal{V}_2(\theta_1, \phi_1, \theta_2, \phi_2; t) = & \beta f(t) (\sin \theta_1 \sin \phi_1 + \sin \theta_2 \sin \phi_2) \\ & + (\sin \theta_1 \sin \theta_2 \cos(\phi_1 - \phi_2) - 2 \cos \theta_1 \cos \theta_2). \end{aligned} \quad (8)$$

In spherical coordinates, the Hamiltonian (7) defines a $(4+1/2)$ -degree-of-freedom dynamical system with coordinates $(\theta_1, \phi_1, \theta_2, \phi_2)$ and the corresponding momenta $(P_{\theta_1}, P_{\phi_1}, P_{\theta_2}, P_{\phi_2})$.

B. Symmetries and invariant manifolds

Since the rotors are identical, Hamiltonians (5) and (7) possess a exchange symmetry. Besides this discrete symmetry, the field-free system, i. e., considering only the dipole interaction and $\beta = 0$, is also invariant under rotations around the common LFF X -axis. Besides the energy, this continuous symmetry implies that the X -component of the total angular momentum $L_X = P_{\phi_1} + P_{\phi_2}$ is conserved.

The Hamiltonian equations of motion arising from (7) read as follows:

$$\begin{aligned} \dot{\theta}_1 &= P_{\theta_1}, \quad \dot{\theta}_2 = P_{\theta_2}, \quad \dot{\phi}_1 = \frac{P_{\phi_1}}{\sin^2 \theta_1}, \quad \dot{\phi}_2 = \frac{P_{\phi_2}}{\sin^2 \theta_2} \\ \dot{P}_{\theta_1} &= \frac{P_{\phi_1}^2 \cos \theta_1}{\sin^3 \theta_1} + \beta f(t) \cos \theta_1 \sin \phi_1 \\ &\quad - \cos \theta_1 \sin \theta_2 \cos \phi_{12} - 2 \sin \theta_1 \cos \theta_2, \\ \dot{P}_{\theta_2} &= \frac{P_{\phi_2}^2 \cos \theta_2}{\sin^3 \theta_2} + \beta f(t) \cos \theta_2 \sin \phi_2 \\ &\quad - \sin \theta_1 \cos \theta_2 \cos \phi_{12} - 2 \cos \theta_1 \sin \theta_2, \\ \dot{P}_{\phi_1} &= \beta f(t) \sin \theta_1 \cos \phi_1 + \sin \theta_1 \sin \theta_2 \sin \phi_{12}. \\ \dot{P}_{\phi_2} &= \beta f(t) \sin \theta_2 \cos \phi_2 - \sin \theta_1 \sin \theta_2 \sin \phi_{12}. \end{aligned} \quad (9)$$

For $\beta = 0$, the infinite set of manifolds \mathcal{M} of codimension four given by

$$\begin{aligned} \mathcal{M} = \{(\theta_1, P_{\theta_1}, \theta_2, P_{\theta_2}) \mid \phi_1 - \phi_2 = 0, \\ \text{and } P_{\phi_1} = P_{\phi_2} = 0; \beta = 0\}. \end{aligned} \quad (10)$$

are invariant under the dynamics. On each of these manifolds, the Hamiltonian (7) for $\beta = 0$ reduces to the two degrees of freedom Hamiltonian

$$\mathcal{H}_{\mathcal{M}} = \frac{P_{\theta_1}^2 + P_{\theta_2}^2}{2} + \sin \theta_1 \sin \theta_2 - 2 \cos \theta_1 \cos \theta_2, \quad (11)$$

and the rotational motion of the dipoles is restricted to a given common polar plane of constant azimuthal inclination $\phi_1 - \phi_2 = 0$ where the polar angles (θ_1, θ_2) vary in the interval $[-\pi, \pi)$. The existence of the manifolds \mathcal{M} is associated to the aforementioned rotational invariance of the Hamiltonian (5) around the LFF X -axis. For $\beta \neq 0$, the electric field breaks this rotational symmetry, and $L_X = P_{\phi_1} + P_{\phi_2}$ is no longer an integral of the motion. It is worth noticing that the presence of the electric field reduces the (infinite) invariant manifolds \mathcal{M} to a single one along the direction $\phi_1 = \phi_2 = 0$, namely

$$\begin{aligned} \mathcal{M}_{XZ} = \{(\theta_1, P_{\theta_1}, \theta_2, P_{\theta_2}) \mid \phi_1 = \phi_2 = 0, \\ \text{and } P_{\phi_1} = P_{\phi_2} = 0\}. \end{aligned} \quad (12)$$

The planar dynamics and the energy transfer on the manifold \mathcal{M}_{XZ} has already been studied in Ref. [18].

The equations of motion (9) provide an additional invariant manifold \mathcal{N} of codimension four,

$$\mathcal{N} = \{(\phi_1, P_{\phi_1}, \phi_2, P_{\phi_2}) \mid \theta_1 = \theta_2 = \pi/2, P_{\theta_1} = P_{\theta_2} = 0\}.$$

When the system is moving on this manifold \mathcal{N} , the dynamics is governed by the $(2 + 1/2)$ -degree-of-freedom Hamiltonian

$$\mathcal{H}_{\mathcal{N}} = \frac{P_{\phi_1}^2}{2} + \frac{P_{\phi_2}^2}{2} - \beta f(t)(\sin \phi_1 + \sin \phi_2) + \cos \phi_{12}.$$

On the manifold \mathcal{N} , the rotational motion of the dipoles is restricted to the parallel $y_1 - z_1$ and $y_2 - z_2$ planes, respectively. This configuration was already considered in Ref. [17] for the general case of a chain of $N \geq 2$ dipoles and zero electric field.

C. Equilibrium configurations

The equilibrium points of a dynamical system provide useful information about its behavior. For $t \geq t_1$, the electric field parameter reaches its maximal value β with $f(t) = 1$, and, using the Cartesian Hamiltonian (5), the equilibrium points are the critical points of the potential

$$\mathcal{V}_1(\mathbf{l}_1, \mathbf{l}_2) = -\beta(z_1 + z_2) + [\mathbf{l}_1 \cdot \mathbf{l}_2 - 3x_1x_2] \quad (13)$$

which is $\mathcal{V}_1(\mathbf{l}_1, \mathbf{l}_2, t)$ (6) with $t \geq t_1$, under the constraints $\{\mathbf{l}_i = (x_i, y_i, z_i) \mid |\mathbf{l}_i|^2 = 1, i = 1, 2\}$, together with the conditions $P_{x_i} = P_{y_i} = P_{z_i} = 0$. Thence, by introducing the Lagrange multipliers λ_1 and λ_2 , the critical points of (13) are the extrema of the Lagrange function \mathcal{V}_L ,

$$\begin{aligned} \mathcal{V}_L(\mathbf{l}_1, \mathbf{l}_2, \lambda_1, \lambda_2) &= \mathcal{V}_1(\mathbf{l}_1, \mathbf{l}_2) \\ &+ \lambda_1(1 - |\mathbf{l}_1|^2) + \lambda_2(1 - |\mathbf{l}_2|^2) \end{aligned} \quad (14)$$

Thus, the critical points are roots of the system of equations $\vec{\nabla}_{x_i, y_i, z_i, \lambda_1, \lambda_2} \mathcal{V}_L = 0$, given by

$$\begin{aligned} x_2 + \lambda_1 x_1 &= 0, & x_1 + \lambda_2 x_2 &= 0, \\ y_2 - 2\lambda_1 y_1 &= 0, & y_1 - 2\lambda_2 y_2 &= 0, \\ z_2 - 2\lambda_1 z_1 - \beta &= 0, & z_1 - 2\lambda_2 z_2 - \beta &= 0, \\ 1 - |\mathbf{l}_1|^2 &= 0, & 1 - |\mathbf{l}_2|^2 &= 0. \end{aligned} \quad (15)$$

In the presence of an electric field ($\beta \neq 0$), the roots of (15) provide the following six sets of (isolated) critical points:

- i) Two critical points P_1 : $z_1 = z_2 = \beta/3$, $y_1 = y_2 = 0$, $x_1 = x_2 = \pm\sqrt{1 - \beta^2/9}$. These points exist when $\beta < 3$ and their energy is $E_1 = -(6 + \beta^2)/3$. In the field-free case, i. e., for $\beta = 0$, they correspond to the well-known stable *head-tail* configurations of the two dipoles along the common LFF X -axis.
- ii) Two critical points P_2 : $z_1 = -z_2 = \pm 1$ and $x_1 = x_2 = y_1 = y_2 = 0$. The energy of these points is $E_2 = -1$ and they exist for values $\beta > 0$.

- iii) The critical point P_3 : $z_1 = z_2 = 1$ and $x_1 = x_2 = y_1 = y_2 = 0$. Its energy is $E_3 = 1 - 2\beta$, and it exists for $\beta > 0$.
- iv) The critical point P_4 : $z_1 = z_2 = -1$ and $x_1 = x_2 = y_1 = y_2 = 0$. The energy of this point is $E_4 = 1 + 2\beta$ and it exists for $\beta > 0$.
- v) Two critical points P_5 : $z_1 = z_2 = -\beta$, $y_1 = y_2 = 0$, $x_1 = -x_2 = \pm\sqrt{1 - \beta^2}$. These points exist when $0 \leq \beta < 1$ and their energy is $E_5 = (2 + \beta^2)$. In the absence of an electric field $\beta = 0$, they correspond to the well-known unstable *tail-tail* or *head-head* configurations of the two dipoles along the common LFF X -axis.
- vi) Two critical points P_6 : $z_1 = z_2 = \beta/2$, $y_1 = -y_2 = \pm\sqrt{1 - \beta^2/4}$, $x_1 = x_2 = 0$. These points exist when $0 \leq \beta < 2$ and their energy is $E_6 = -(2 + \beta^2)/2$.

In contrast, for the field-free case $\beta = 0$, the number of critical points reduces to P_1 and P_5 , and to two degenerate circles of equilibria D_1 and D_2 :

- The set D_1 is given by $z_1 = z_2 = \cos \alpha$, $y_1 = y_2 = \sin \alpha$, $x_1 = x_2 = 0$, with $\alpha = [0, 2\pi)$. The energy of this circle of stationary points is $E_3 = 1$, and, when $\beta = 0$, the former isolated critical points P_3 and P_4 for $\beta \neq 0$ are included in D_1 .
- The set D_2 is given by $z_1 = -z_2 = \cos \alpha$, $y_1 = -y_2 = \sin \alpha$, $x_1 = x_2 = 0$, with $\alpha = [0, 2\pi)$. The energy of these equilibria is $E_4 = -1$, and, when $\beta = 0$, the former isolated equilibria P_2 and P_6 for $\beta \neq 0$ are included in D_2 .

A detailed study of the stability and existence of the critical points as well as their bifurcations as β is varied is provided in the Appendix.

Let us explain the differences between the equilibria of the full 3D system and when the dynamics is restricted to the planar manifold \mathcal{M}_{XZ} [18]. For $\beta = 0$, there are two isolated equilibria $P_{1,5}$ and the degenerate circles of equilibria $D_{1,2}$; whereas on the manifold \mathcal{M}_{XZ} , there are five isolated equilibria $P_{1,2,3,4,5}$. For $\beta \neq 0$, all the equilibria are isolated, such that in the 3D system there appears an additional equilibrium P_6 located off the manifold \mathcal{M}_{XZ} .

III. ENERGY TRANSFER PROCESSES

In this section, we explore the classical dynamics of the two dipoles in an external electric field. We assume that initially at $t = 0$, the two dipoles are at rest, with zero kinetic

energy, in the stable *head-tail* configuration along the LFF X -axis given by the equilibrium points P_1 . In this state, the system has the minimal energy $E_1 = -2$. From this initial configuration, the field is turned on at $t = 0$ by the ramp-up function (3), and a certain excess energy δK is given to dipole one. Therefore, taking into account the holonomic constraints $\{\mathbf{l}_i = (x_i, y_i, z_i) \mid |\mathbf{l}_i|^2 = 1, i = 1, 2\}$, the system leaves the stable equilibrium configuration in such a way that, at $t = 0$, the initial conditions of the dipoles are

$$\begin{aligned} x_1(0) &= x_2(0) = 1, & y_1(0) &= y_2(0) = z_1(0) = z_2(0) = 0 \\ P_{y_1}(0) &= \sqrt{2\delta K} \cos \alpha, & P_{z_1}(0) &= \sqrt{2\delta K} \sin \alpha, \\ P_{x_1}(0) &= P_{x_2}(0) = P_{y_2}(0) = P_{z_2}(0) = 0. \end{aligned} \quad (16)$$

The angle $\alpha \in [-\pi, \pi)$ allows us to consider all possible directions of rotations perpendicular to the head-tail axis, and all initial conditions of its momentum. Using the initial conditions (16), the equations of motion given by the Hamiltonian (5) are numerically integrated up to a final time t_f by means of the so-called Störmer-Verlet algorithm [27]. This numerical algorithm is a symplectic integrator that preserves the holonomic constraints of the system. The final integration time is fixed to $t_f = 400$. Our numerical tests have shown that this stopping or final time is appropriate for a proper characterization of the outcomes. In particular, for a LiCs molecule in its ground state trapped in an optical lattice with $a_l = 450$ nm, the time unit is $t_d = \sqrt{I/\chi} \approx 6.5$ ns, and the final time $t_f = 400 \approx 2500$ ns. The ramp-up time is fixed to $t_1 = 2$, that roughly corresponds to 12 ns and that can be achieved in current experiments with realistic field strengths.

For these initial conditions, we explore the dynamics of this system for different ratios of the electric field interaction and the dipole-dipole one, specifically $\beta = 0, 0.1, 1, 10, 100, 1000$. To do so, we compute the normalized time-average of the kinetic energy of each dipole, \widehat{K}_i , given by

$$\widehat{K}_i = \frac{\langle K_i \rangle}{\langle K_1 \rangle + \langle K_2 \rangle}, \quad (17)$$

with

$$\langle K_i \rangle = \frac{1}{2t_f} \int_0^{t_f} [P_{x_i}^2(t) + P_{y_i}^2(t) + P_{z_i}^2(t)] dt, \quad (18)$$

where t_f is the final time. In the presence of the electric field, the axial symmetry no longer exists and the dipoles tend to orient along the electric field direction. We characterize their

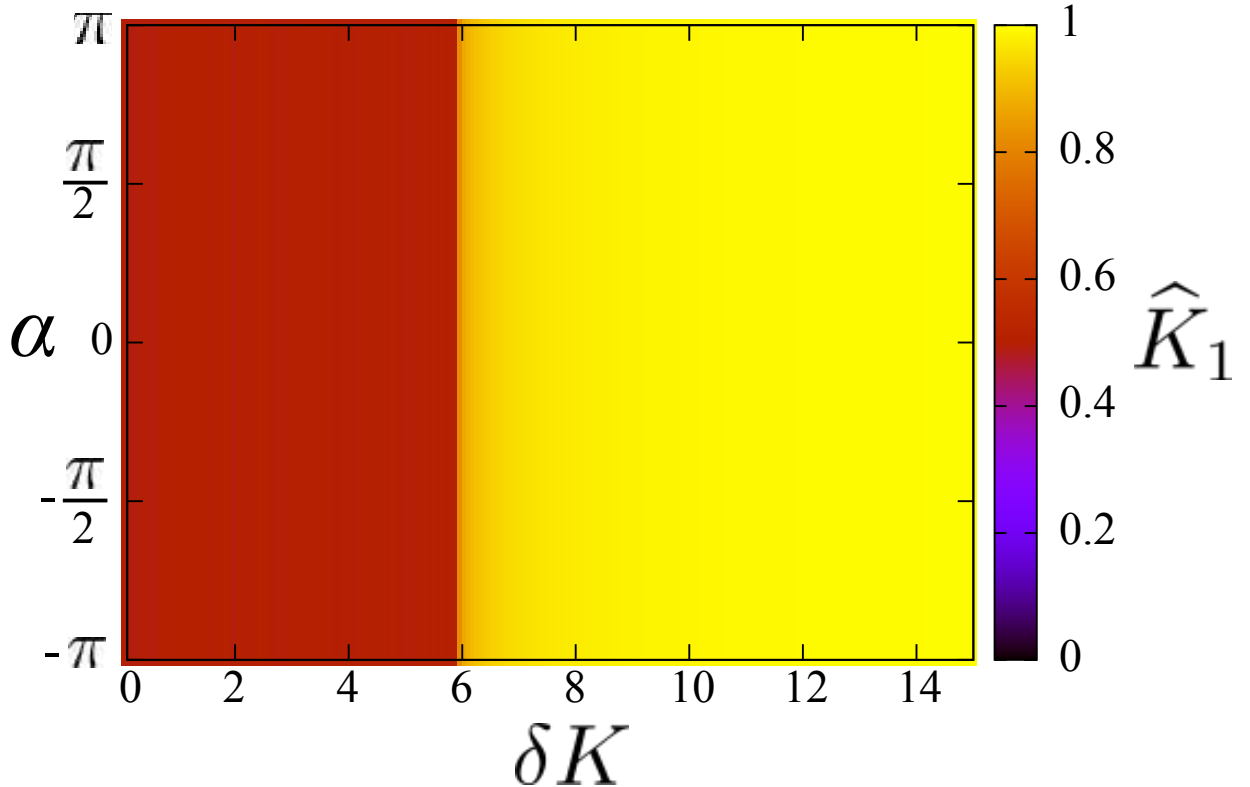


FIG. 2. Normalized time-averaged kinetic energy \widehat{K}_1 of the first dipole, for $\delta K \in [0.1, 15]$ and $\alpha \in [-\pi, \pi)$, in the field-free case $\beta = 0$.

orientations by computing the time-average of the Cartesian coordinate z_i

$$\langle z_i \rangle = \frac{1}{t_f} \int_0^{t_f} z_i(t) dt, \quad i = 1, 2. \quad (19)$$

Computationally, these time-averaged quantities \widehat{K}_i and $\langle z_i \rangle$ are easily calculated as a function of the kinetic energy δK given to dipole one and of the angle α with which this dipole begins to rotate. However, from a realistic perspective, this angle is difficult to be externally controlled. In this way, we also compute the averages of \widehat{K}_i and $\langle z_i \rangle$ over all possible realizations of this angle α . These α -averaged quantities $\langle \widehat{K}_i \rangle_\alpha$ and $\langle z_i \rangle_\alpha$ provide insight, as a function of the excess energy δK , into the global extent of the energy equipartition and the orientation of the dipoles, respectively.

Let us start analyzing the field-free system, i. e., $\beta = 0$. The dynamics depends on δK , which is the excess kinetic energy given to the system, and on the angle α . The normalized time-averaged kinetic energy of the dipole one is presented in Fig. 2 for $0 \leq \delta K \leq 15$ and $\alpha \in [-\pi, \pi)$. According to this color map, the kinetic energy transfer between the dipoles

does not depend on α , that is, on the direction in which the first dipole begins to rotate. In the initial state both dipoles are aligned along the symmetry axis of the field-free system, the LFF X -axis, which is the generatrix of the invariant manifolds \mathcal{M} . Since the excess kinetic energy is added to one of the dipoles, the system will be always moving on one of these invariant manifolds \mathcal{M} . As the dynamics on these manifolds \mathcal{M} is equivalent, due to the rotational symmetry around the LFF X -axis, the direction in which dipole one starts to rotate has no impact on the global dynamics. Thus, the normalized time-averaged kinetic energy is independent of α , as it is shown in Fig. 2.

For an excess energy δK smaller than the critical value $\delta K_c \approx 6$, Fig. 2 shows that the system always reaches the equipartition energy regime, $\langle K_1 \rangle$ is very close to $\langle K_2 \rangle$, and a continuous energy flow between the rotors occurs. For $\delta K \approx 6$, this equipartition regime abruptly breaks, so that most of the kinetic energy remains always in dipole one for $\delta K \gtrsim 6$. As a consequence, the equipartition energy regime inside the invariant manifolds \mathcal{M} applies only for low values of the excess energy $\delta K < \delta K_c$. This feature was detected in Ref. [17]. The authors provided a dynamical explanation of this phenomenon in [18] when they studied the energy transfer only in the invariant manifold \mathcal{M}_{XZ} given by (12). Let us emphasize that taking into account all the invariant manifolds \mathcal{M} , Fig. 2 proves that the system exhibits the same feature in all of them, as they are dynamically equivalent due to the field-free axial symmetry.

For a weak electric field, the electric field interaction can be considered as a perturbation to the dipole-dipole one. Indeed, for $\beta = 0.1$, the normalized time-averaged kinetic energy of dipole one \widehat{K}_1 in Fig. 3(a) shows qualitatively a similar behaviour as the field-free results of Fig. 2, except for a region around the critical value $\delta K_c = 6$. Thence, for $\delta K \lesssim 6$, the system reaches the equipartition regime, while for $\delta K \gtrsim 6$ most of the kinetic energy remains stored in dipole one. It is worth noticing that, in the neighborhood of $\delta K_c \approx 6$, the time-averaged \widehat{K}_1 shows sudden (irregular) variations, which indicate that in this region the system is very sensitive to the initial conditions, i. e., to the values of δK and α . The evolution of $\langle z_1 \rangle$ depicted in Fig. 3(b) indicates that this weak electric field $\beta = 0.1$ does not cause any significant orientation in dipole one. In contrast, for $\delta K \gtrsim 6$, the color map of Fig. 3(c) shows regions of initial conditions leading to a moderate orientation of the dipole two along the electric field with $\langle z_2 \rangle \approx 0.5$, see the light brown regions of Fig. 3(c). A correlation between the behaviors of \widehat{K}_i and $\langle z_i \rangle$ arises when the α -averaged $\langle \widehat{K}_i \rangle_\alpha$ and $\langle z_i \rangle_\alpha$

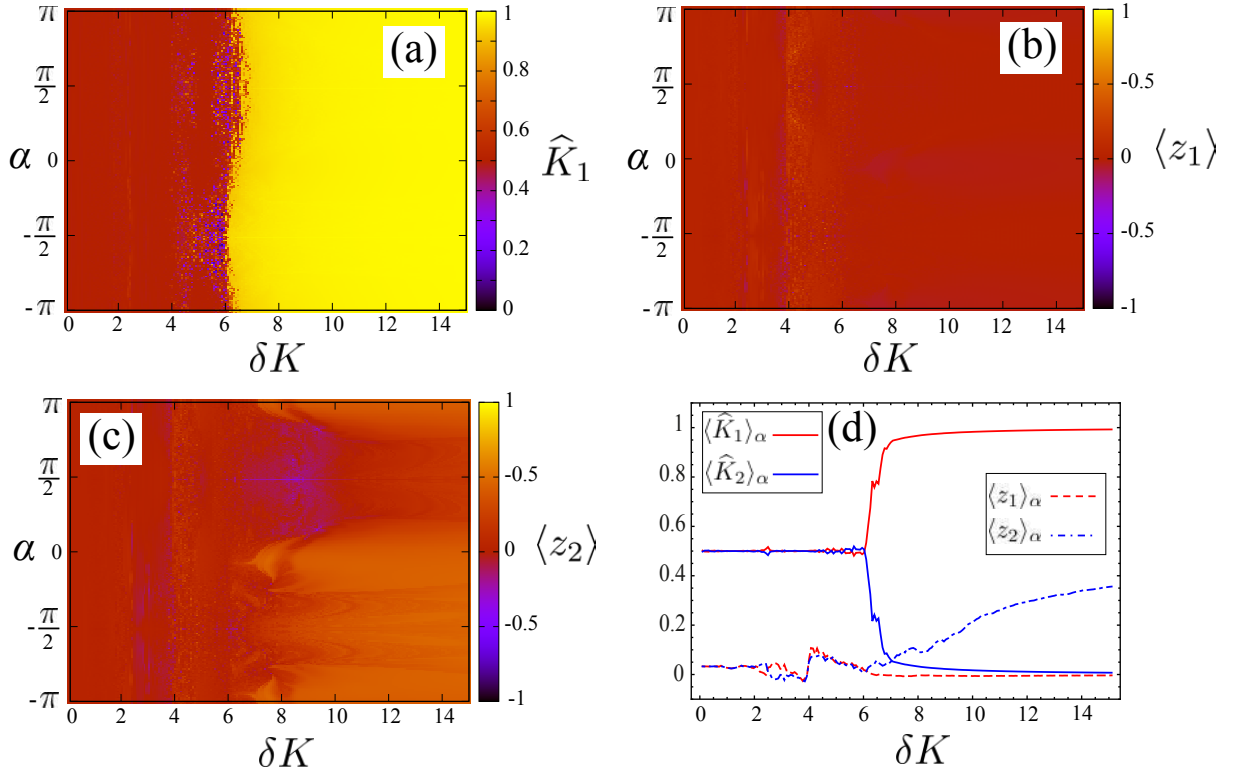


FIG. 3. (a) Normalized time-averaged kinetic energy \widehat{K}_1 of the first dipole. (b)-(c) Time averages $\langle z_1 \rangle$ and $\langle z_2 \rangle$, respectively. (d) The α -averaged $\langle \widehat{K}_i \rangle_\alpha$ and $\langle z_i \rangle_\alpha$ over the internal distribution angle α . For all panels, the electric field parameter is $\beta = 0.1$.

are analyzed in Fig. 3(d). While the system is in the equipartition region, i. e., $\delta K \lesssim 6$, the orientation of both dipoles is negligible $\langle z_i \rangle_\alpha \approx 0$. However, in the region $\delta K \gtrsim 6$ where most of the kinetic energy is in dipole one, the α -averaged orientation $\langle z_2 \rangle_\alpha$ of dipole two begins to increase monotonically with δK , whereas the dipole one remains non-oriented $\langle z_1 \rangle_\alpha \approx 0$. This behavior is expected because in the non-equipartition regime most of the kinetic energy is stored in dipole one, which swings very fast compared to dipole two. Thence, dipole two is more likely to be oriented along the field than dipole one.

Now, we analyze the dynamics when the dipole-dipole and the electric field interactions are of the same order of magnitude, specifically we take $\beta = 1$. The corresponding results are shown in Fig. 4. Roughly speaking, for $\delta K \lesssim 8$ the system eventually relaxes to equipartition, see Fig. 4(a). Whereas, for $\delta K \gtrsim 8$ the system progressively moves away from equipartition, and as δK increases, most of the kinetic energy remains in the initially excited

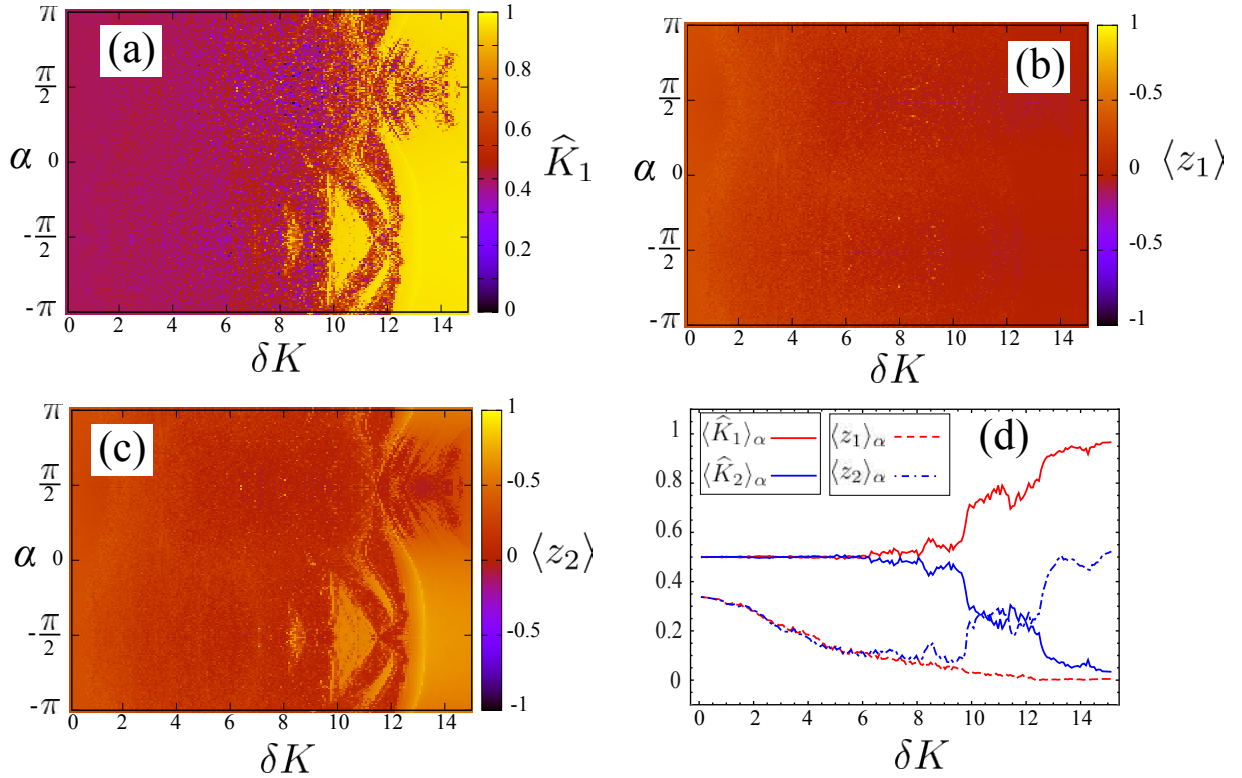


FIG. 4. (a) Normalized time-averaged kinetic energy \widehat{K}_1 of the first dipole. (b)-(c) Time averages $\langle z_1 \rangle$ and $\langle z_2 \rangle$, respectively. (d) The α -averaged $\langle \widehat{K}_i \rangle_\alpha$ and $\langle z_i \rangle_\alpha$ over the internal distribution angle α . All the panels for an electric field parameter $\beta = 1$.

dipole one. For $\delta K \gtrsim 8$, it is worth noticing the remarkable complex behavior observed in the evolution of \widehat{K}_1 in Fig. 4(a), i. e., the dynamics shows a high sensitivity to the initial conditions δK and α . This feature will be addressed in the next section. For $\delta K \lesssim 8$, there is no remarkable difference in the orientations of the dipoles in Fig. 4(b)-(c). We only highlight the slight orientation of both dipoles for small values of δK , see the light brown regions in Figs. 4(b)-(c) for $\delta K \lesssim 2$. By further increasing the excess energy, $\delta K \gtrsim 8$, the orientation of each dipole evolves differently. While the orientation of dipole one slightly decreases for increasing δK , see Fig. 4(b), there are regions in Fig. 4(c) where the orientation of the dipole two presents a significant increase. Furthermore, Figs. 4(a) and (c) show similar patterns, which confirm a clear correlation between the non-equipartition regime with most of the kinetic energy in dipole one, and dipole two having a larger orientation.

The evolutions of the α -averaged $\langle \widehat{K}_i \rangle_\alpha$ and $\langle z_i \rangle_\alpha$ depicted in Fig. 4(d) show that, indeed, there is equipartition up to $\delta K \lesssim 8$. For this situation, $\langle z_1 \rangle_\alpha$ and $\langle z_2 \rangle_\alpha$ are equal and take the

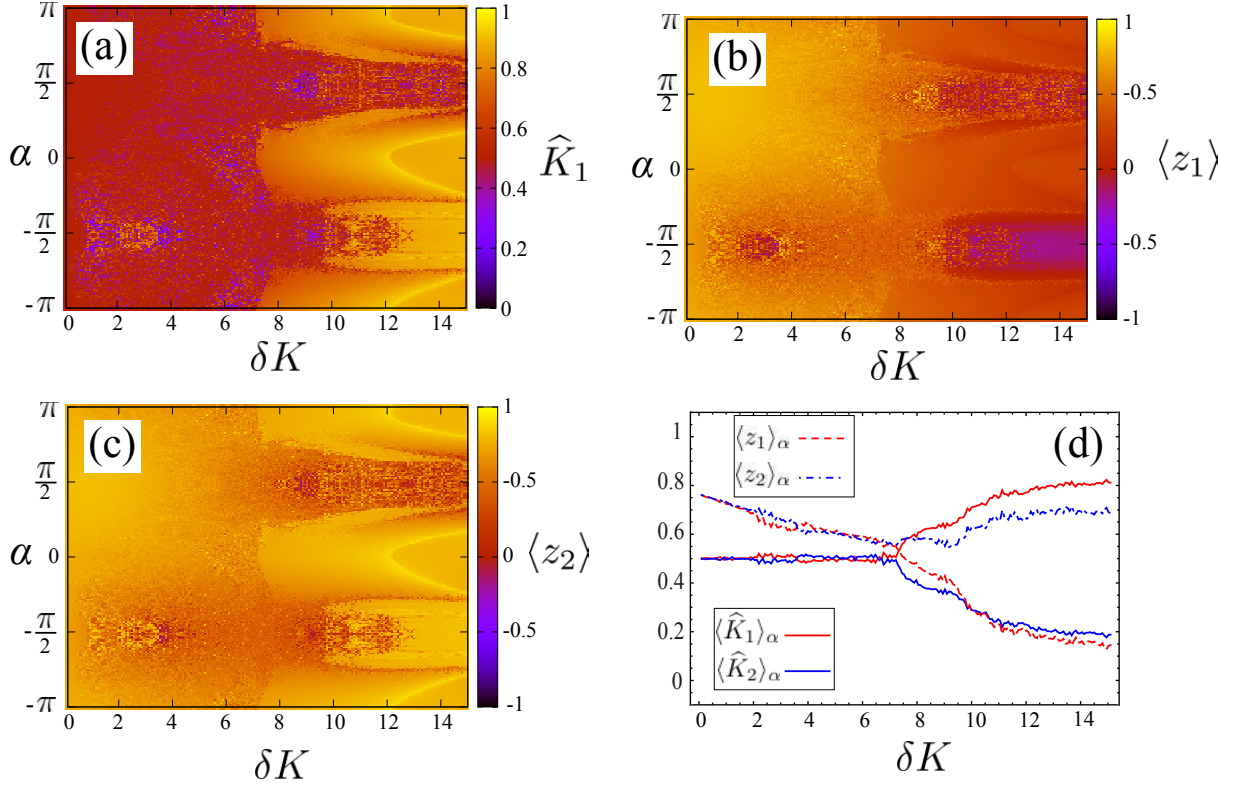


FIG. 5. (a) Normalized time-averaged kinetic energy \widehat{K}_1 of the first dipole. (b)-(c) Time averages $\langle z_1 \rangle$ and $\langle z_2 \rangle$, respectively. (d) $\langle \widehat{K}_i \rangle_\alpha$ and $\langle z_i \rangle_\alpha$ averaged with respect to the internal distribution angle α . $\beta = 10$ holds for all the figures.

maximal orientation for small excess energy values, and they have very similar values and decrease monotonically for increasing δK . When the equipartition regime is lost for $\delta K \gtrsim 8$, the evolutions of the α -averaged $\langle \widehat{K}_1 \rangle_\alpha$ and $\langle \widehat{K}_2 \rangle_\alpha$, red and blue solid lines in Fig. 4(d), respectively, indicate a gradual but non-monotonic growth of the kinetic energy of dipole one at expense of the one of dipole two. At the same time, $\langle z_1 \rangle_\alpha$ continues decreasing for increasing δK , whereas, analogously to $\langle \widehat{K}_1 \rangle_\alpha$, $\langle z_2 \rangle_\alpha$ non-monotonically increases.

Now, we increase the electric field strength up to $\beta = 10$, i. e., the electric field interaction is one order of magnitude larger than the dipole-dipole one, the corresponding results are presented in Fig. 5. In the color map of Fig. 5(a), we encounter that most of the initial conditions lead the systems to equipartition for $\delta K \lesssim 7$. Analogously to the $\beta = 1$ dynamics, a more complex behavior appears for $\delta K \gtrsim 7$. Except for a region around $\alpha = \pi/2$, the energy transfer mechanism is dominated by a non-equipartition regime, and most of the initial excess energy δK remains in dipole one. Although in this region around $\alpha = \pi/2$

the equipartition regime is dominant, there exist regions of initial conditions that lead to non-equipartitioning.

The time-averaged inclinations $\langle z_1 \rangle$ and $\langle z_2 \rangle$ shown in Figs. 5(b)-(c) present similar patterns as those observed for \widehat{K}_1 in Fig. 5(a). In the region dominated by energy equipartition $\delta K \lesssim 7$, the maps of Figs. 5(b)-(c) indicate that the dipoles are significantly oriented along the electric field axis. For $\delta K \gtrsim 7$, the orientation of dipole one in Fig. 5(b) decreases as δK increases, and around $\alpha = -\pi/2$, there are initial conditions leading even to antiorientation, which correspond to this dipole having most of the energy in Fig. 5 (a). In contrast, the orientation of dipole two is globally enhanced in the non-equipartition region $\delta K \gtrsim 7$, see Fig. 5(c). Only for initial conditions in the region around $\alpha = \pi/2$ both dipoles have similar orientations slightly directed towards the electric field. In other words, when the dipole one begins to rotate in the direction of the electric field and equipartition is dominant, the dipoles end up having enough energy to prevent their orientation. That is, for initial conditions around $\alpha = \pi/2$, the non-equipartition regime existing in the absence of the electric field $\beta = 0$ for $\delta K \gtrsim 6$, see Fig. 2, is mostly broken when the field is switched on. In contrast, for initial conditions out of that region, the system tends to remain in the same non-equipartitioning regime exhibited in the absence of the electric field, with most of the energy in dipole one. Thus, the electric field interaction is still not able to relax the system out of the non-equipartition regime, and, therefore, only the second dipole is significantly oriented by the electric field.

Again, the δK -evolution of the α -averaged quantities in Fig. 5(d) confirms the behavior of the time-averaged ones presented in Figs. 5(a)-(c). During the equipartition regime for $\delta K \lesssim 7$ the dipoles have similar orientation. This orientation is maximal for small values of δK and decreases as δK increases. For $\delta K \gtrsim 7$, $\langle z_1 \rangle_\alpha$ continues decreasing because most of the energy is stored in dipole one, whereas $\langle z_2 \rangle_\alpha$ grows slightly for increasing δK .

By further increasing the electric field to $\beta = 100$, the dynamics is dominated by the interaction with the electric field. In Fig. 6(a), the normalized time-averaged kinetic energy \widehat{K}_1 shows a complex behavior strongly depending on the initial excess energy δK and on the angle α . The map of Fig. 6(a) shows wide regions of energy equipartition. Interestingly, there is a blue-colored (brown-colored) area centered around $\alpha = \pi/2$ ($\alpha = -\pi/2$) where most of the kinetic energy is stored in dipole two (one). This means that when dipole one starts to rotate on an axis perpendicular to its $x_1 z_1$ plane, the equipartition regime is not

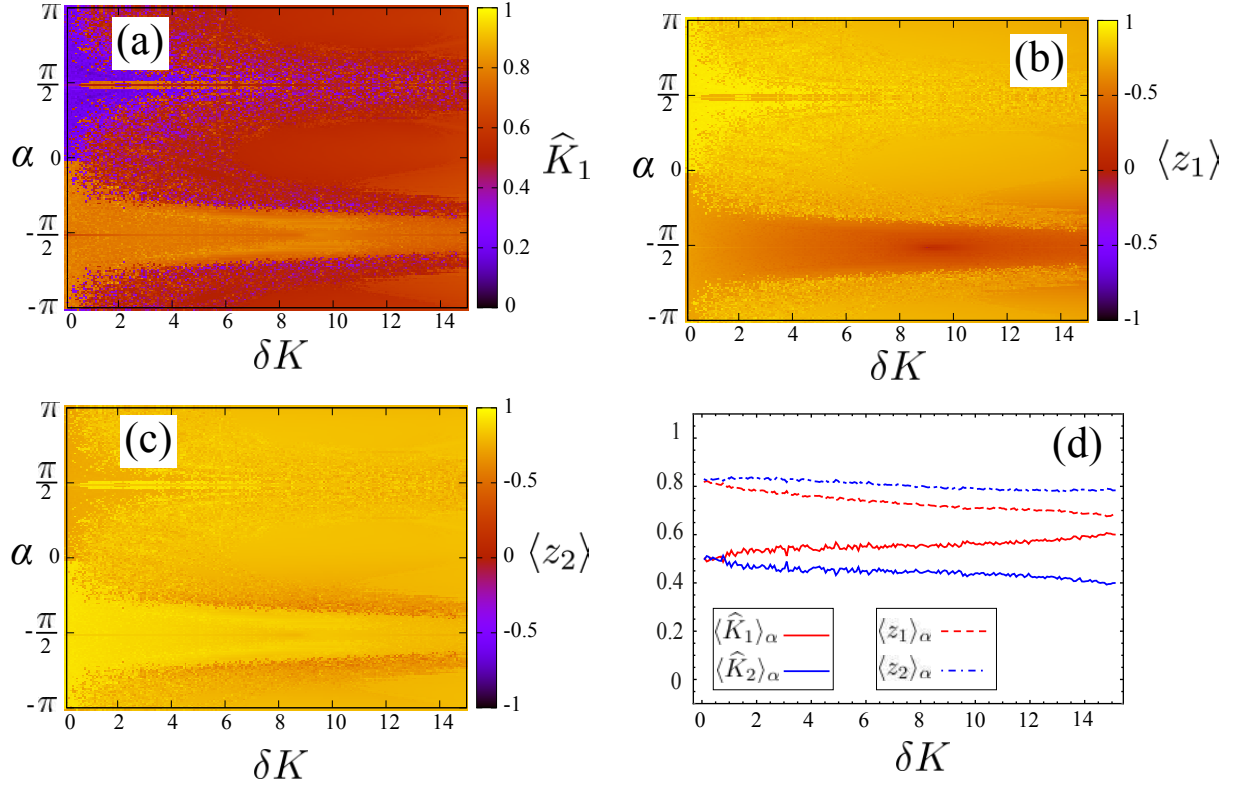


FIG. 6. (a) Normalized time-averaged kinetic energy \widehat{K}_1 of the first dipole. (b)-(c) Time averaged $\langle z_1 \rangle$ and $\langle z_2 \rangle$, respectively. (d) $\langle \widehat{K}_i \rangle_\alpha$ and $\langle z_i \rangle_\alpha$ averaged with respect to the internal distribution angle α . All the panels are for an electric field parameter $\beta = 100$.

reached. For this strong electric field, a substantial orientation of the dipoles is expected, which is confirmed by the large values of $\langle z_1 \rangle$ and $\langle z_2 \rangle$ in Fig. 6(b)-(c). Regardless of this orientation, Figs. 6(b) and (c) present similar structures as Fig. 6(a), as was previously observed for $\beta = 1$ and 10. Thus, the non-equipartition regions in Fig. 6(a) with most of the kinetic energy located in one of the dipoles correspond to the lighter and darker red colored regions of Figs. 6(b)-(c), where the orientation is minimal and maximal, respectively. The α -averaged $\langle \widehat{K}_1 \rangle_\alpha$ and $\langle \widehat{K}_2 \rangle_\alpha$ of Fig. 6(d) confirm that the system is always near equipartition, with a small positive energy balance for dipole one. Due to the strong electric field $\beta = 100$, $\langle \widehat{K}_1 \rangle_\alpha$ and $\langle \widehat{K}_2 \rangle_\alpha$ show just a slight variation as δK increases. A similar situation is found for the α -averaged $\langle z_i \rangle_\alpha$, where the large orientation induced by the field is only slightly counteracted for increasing initial energy δK . Again, the less energetic dipole two is more oriented than the more energetic dipole one.

When the electric field interaction is three order of magnitude larger than the dipole-

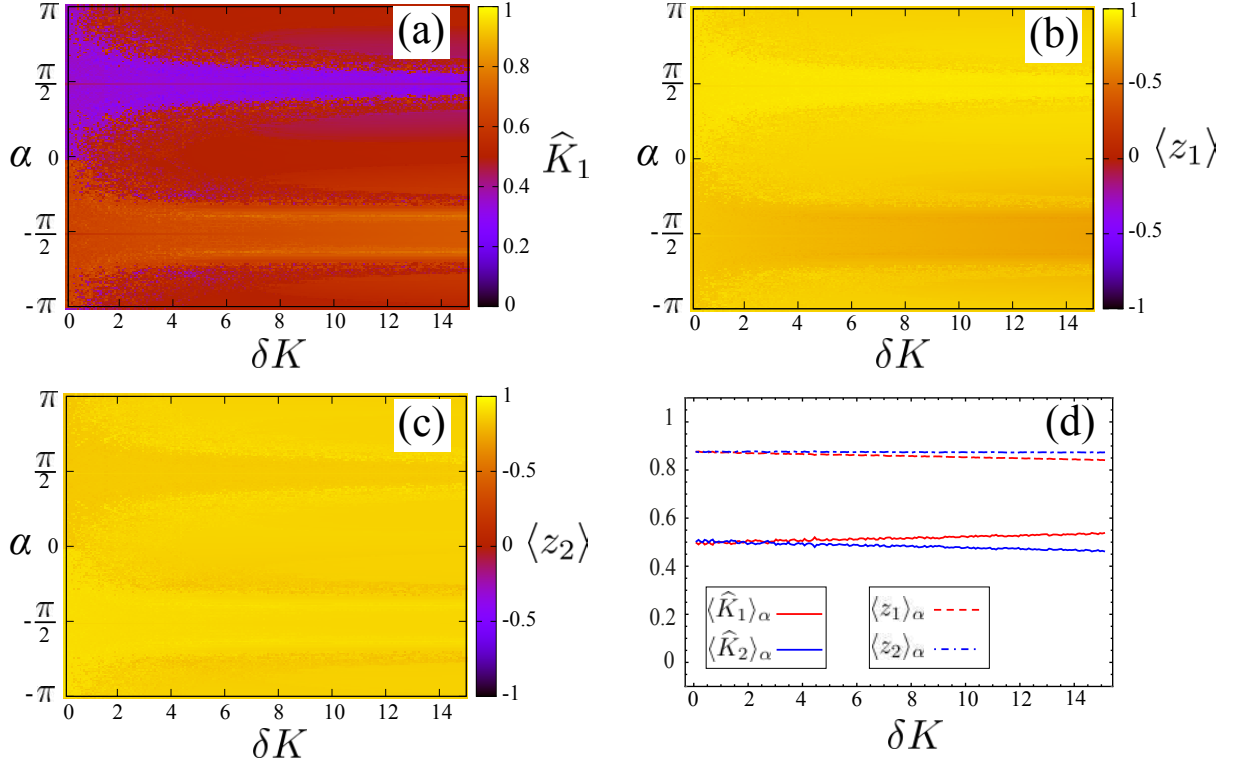


FIG. 7. (a) Normalized time-averaged kinetic energy \widehat{K}_1 of the first dipole. (b)-(c) Time averages $\langle z_1 \rangle$ and $\langle z_2 \rangle$, respectively. (d) $\langle \widehat{K}_i \rangle_\alpha$ and $\langle z_i \rangle_\alpha$ averaged with respect to the internal distribution angle α . All the panels are for an electric field parameter $\beta = 1000$.

dipole one i.e., $\beta = 1000$, most of the initial conditions leave the system close to the equipartition regime see Fig. 7(a). Moreover, the normalized time-averaged kinetic energy \widehat{K}_1 and the orientations show similar behaviours as those for the $\beta = 100$ case, compare Figs. 6(a)-(b)-(c) and Figs. 7(a)-(b)-(c). We again encounter the non-equipartition regions around $\alpha = \pi/2$ and $-\pi/2$, where most of the kinetic energy is stored in dipole two and one, respectively. Thus, the energy equipartition regime is closely related to a smaller orientation of dipole two and viceversa. However, due to the strong electric field the two dipoles are significantly oriented along the electric field direction, see Figs. 7(b)-(c). The α -averaged $\langle \widehat{K}_i \rangle_\alpha$ and $\langle z_i \rangle_\alpha$ of Fig. 7 assert that the system is always close to the equipartition regime, whereas the strong field orients the dipoles with $\langle z_i \rangle_\alpha > 0.8$ with $i = 1, 2$.

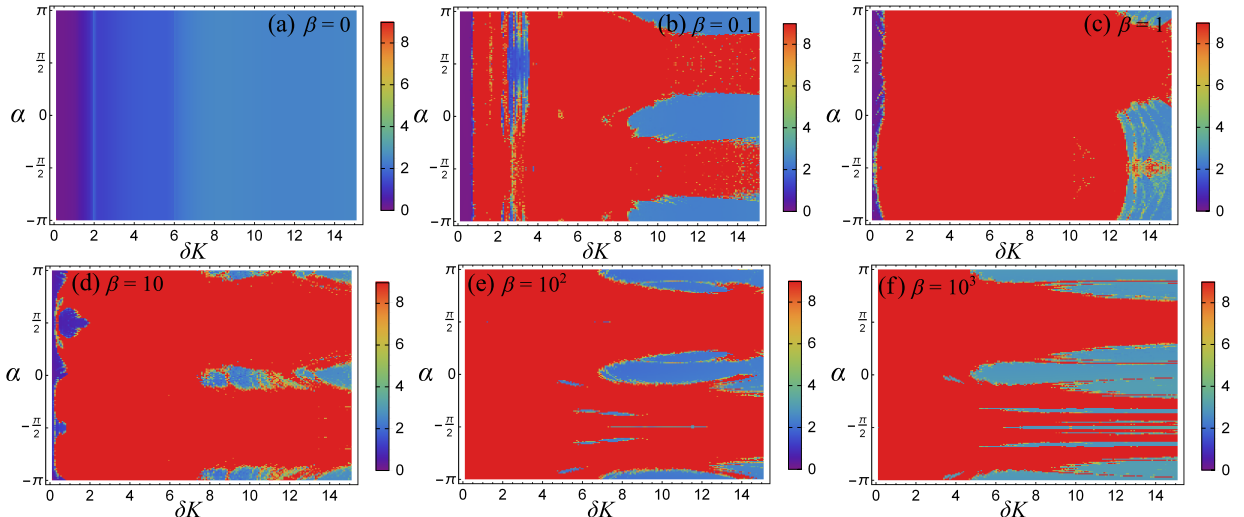


FIG. 8. FLI values for different initial conditions with $\delta\mathcal{K} \in [0.1, 15]$ and $\alpha \in [-\pi, \pi)$.

IV. REGULAR AND CHAOTIC DYNAMICS

In this section, we study the chaoticity of the dynamics and its possible relation to the time-averaged energy transfer. The chaotic character of an orbit in a dynamical system is related to its sensitivity to the corresponding initial conditions. As a numerical measure of this sensitivity, we use the so-called, Fast Lyapunov Indicator (FLI) [28–30] to determine the degree of chaoticity of an orbit. Given a n -dimensional flow of a dynamical system

$$\frac{d\mathbf{r}}{dt} = \mathbf{f}(\mathbf{r}, t), \quad (20)$$

the time evolution of the variational vector $\delta\mathbf{r}(t)$ is provided by the variational equation

$$\frac{d\delta\mathbf{r}}{dt} = \frac{\partial\mathbf{f}(\mathbf{r}, t)}{\partial\mathbf{r}} \delta\mathbf{r}. \quad (21)$$

For a given orbit with initial conditions $\mathbf{r}(0)$ and $\delta\mathbf{r}(0)$, the numerical integration of equations (20) and (21) up to a final time t_f yields the value of the FLI of that orbit defined by

$$\text{FLI}(\mathbf{r}(0), \delta\mathbf{r}(0), t_f) = \sup_{0 \leq t \leq t_f} \log \|\delta\mathbf{r}(t)\|. \quad (22)$$

The variational vector $\delta\mathbf{r}$ increases linearly with time for regular periodic and quasiperiodic orbits, whereas it increases exponentially for chaotic orbits.

We have calculated FLI for varying initial conditions $\delta\mathcal{K}$ and α . To do so, we have integrated the equations of motion and their first variational equations in Cartesian coordinates

by means of the Störmer-Verlet algorithm [27] using the same initial conditions as in the previous section. Now, we stop the integration if the FLI reaches the saturation value nine, that characterizes an orbit as chaotic, or if the integration time reaches the stopping value $t_f = 3000$. Our numerical tests have shown that this stopping time and saturation limit are adequate to correctly characterize any orbit.

The FLI color maps are presented in Fig. 8 for the electric field strengths $\beta = 0, 0.1, 1, 10, 100$ and 1000, the initial kinetic energy excess $\delta\mathcal{K} \in [0, 15]$ and the angle $\alpha \in [-\pi, \pi)$. It is worth noting that, along the horizontal lines $\alpha = 0$ and $\alpha = \pm\pi$ in Fig. 8, the system evolves on the invariant manifold \mathcal{M} given by the planes $y_1 = y_2 = 0$, i. e., both dipoles are restricted to rotate in the common $x_1z_1 \equiv x_2z_2$ plane.

In the absence of the electric field, $\beta = 0$, we observe in Fig. 8(a) that the FLI values do not depend on the angle α , that is, on the direction in which the first dipole begins to rotate. As explained above, this is because regardless of the value of α , the system will always move in one of the equivalent invariant manifolds \mathcal{M} . Moreover, for zero electric field, the FLI value increases with the kinetic energy excess $\delta\mathcal{K}$, although the dynamics is regular for all initial conditions. By switching on the electric field, most of the dynamics becomes chaotic even for weak electric fields such as $\beta = 0.1$, see Fig. 8(b). For electric field values up to $\beta = 10$, the regular behavior only persists for low values of the kinetic energy excess $\delta\mathcal{K} < 1$ and particularly around $\alpha = 0$ and $\alpha = \pm\pi$, see Figs. 8(b-d). For stronger electric fields, the chaotic behavior of the system still persists in wide regions of the FLI maps Fig. 8(e-f) for $\beta = 100$ and 1000 and for the range of $\delta\mathcal{K}$ values shown. This is somehow an unexpected result because for increasing field strength the dynamics is gradually dominated by the interaction of the dipoles with the field. This would lead the system to a (quasi) integrable regime, where most of the dynamics would be regular. However, the dipolar interaction, although being small compared to the electric field interaction, it is still able to cause a substantial volume of chaotic motion. In this sense, we have calculated the FLI maps in the range $0 < \delta\mathcal{K} \leq 15$ for very large values of the field parameter, namely for $\beta = 10^5$ and 10^6 (see Fig.9). Indeed, we observe in the color maps of Fig.9. that, for increasing values of β , the regions of initial conditions leading to regular motion grow in size while the regions of initial conditions leading to chaotic orbits shrink. However, this global tendency to regular motion is very slow, which confirms the relevant role that the DDI is playing in the dynamics even for very large electric field values.

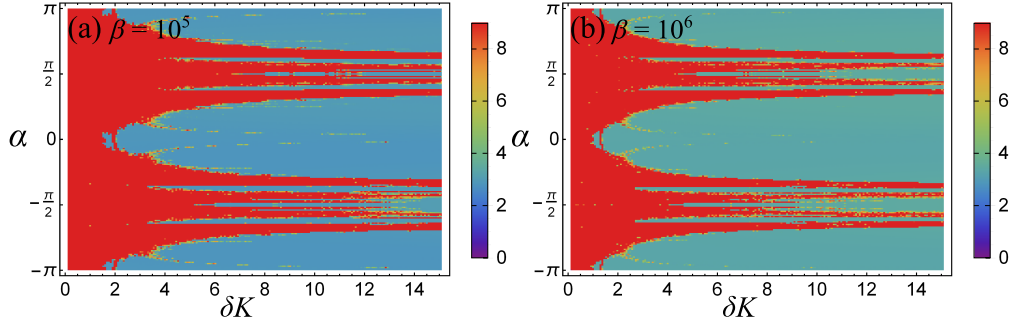


FIG. 9. FLI values for different initial conditions with $\delta K \in [0.1, 15]$ and $\alpha \in [-\pi, \pi)$ for (a) $\beta = 10^5$ and (b) $\beta = 10^6$.

A comparison of the results obtained for the time-averaged energy transfer, see Figs. 3-7, with those for the degree of chaoticity presented in Fig. 8 does not show any significant correlation. This may be due to the fact that regular and chaotic orbits can achieve the same time-averaged kinetic energy. We have additionally computed another chaos indicator, the so called Smaller Alignment Index (SALI) [31, 32], and the corresponding results are in perfect agreement with the FLI ones presented here.

V. CONCLUSIONS

We have theoretically investigated two interacting classical dipoles fixed in space, which are described as rigid rotors, in the presence of a homogenous electric field. The two dipoles are initially at rest in the stable head-tail configuration. Initially, one of the dipoles is pushed out of this stable configuration by giving it a specific velocity in a direction perpendicular to the head-tail axis, and at the same time the electric field is switched on. The following classical dynamics is explored in terms of the energy transfer mechanisms between the two dipoles and their orientations along the electric field axis.

The field-free dynamics of this system was previously investigated in the invariant manifold \mathcal{M}_{XZ} (12) in Ref. [18]. Here, we have shown that the dynamics is independent of the initial rotation angle of the dipole because it is restricted to one of the invariant manifolds of the infinite set \mathcal{M} . Depending on the initial excess energy given to one of the dipoles, the system falls to either an energy equipartition regime or a non-equipartition one, and the dynamics is regular.

The classical field-dressed dynamics strongly depends on the electric field strength and on

the initial conditions. For weak external fields, the dynamics is still dominated by the dipole-dipole interaction and the energy transfer dynamics resembles the field-free dynamics with the two dipoles having a small orientation. By increasing the electric field, the interaction with this field dominates the classical dynamics. The size of the non-equipartition region appearing for large values of the initial excess energy decreases as the electric field increases, and the system tends to the energy equipartition regime. In addition, the orientation of the two dipoles along the electric field direction increases. We note that when the initial momentum is almost parallel or antiparallel to the electric field direction, we observe that even for very strong electric fields, the non-equipartition behavior dominates the dynamics. Finally, we find that, even for large electric field strengths and for our considered excess energies, the system shows a highly chaotic behavior. This is a remarkable feature because for increasing electric field strength it would be expected that the system gradually tends to a (quasi) integrable state where the dynamics is fully dominated by the interaction of the dipoles with the field and where the mutual dipole interaction would be considered as a small perturbation. However, as we have observed for very large values of the electric field, the DDI is still able to generate significant regions of chaotic motion.

A natural continuation of this work would be the investigation of the energy transfer and the possible collective phenomena of systems with many 3D-dipoles including in particular, the study of a linear chain of 3D-dipoles.

ACKNOWLEDGMENTS

M.I. and J.P.S. acknowledge financial support by the Spanish Project No. MTM 2017-88137-C2-2-P (MINECO). R.G.F. gratefully acknowledges financial support by the Spanish Project No. FIS2017-89349-P (MINECO), and by the Andalusian research group FQM-207. This study has been partially financed by the Consejería de Conocimiento, Investigación y Universidad, Junta de Andalucía and European Regional Development Fund (ERDF), Ref. SOMM17/6105/UGR.

Table I. Conditions of existence, stability and energy of the critical points of $\mathcal{V}_1(\mathbf{l}_1, \mathbf{l}_2)$ in Eq. (13). The acronyms SPR1, SPR2 and SPR3 denote saddle points of rank-one, rank-two and rank-three, respectively.

Equilibria	Existence	Stability	Energy \mathcal{E}
D_1	$\beta = 0$	Degenerate circle of equilibria	$E_{D_1} = 1$
D_2	$\beta = 0$	Degenerate circle of equilibria	$E_{D_2} = -1$
P_1	$\beta < 3$	Minima	$E_1 = -(6 + \beta^2)/3$
P_2	$\beta > 0$	SPR2	$E_2 = -1$
P_3	$\beta > 0$	If $0 < \beta < 2$: SPR2; if $2 < \beta < 3$: SPR1; If $\beta > 3$: Minima	$E_3 = 1 - 2\beta$
P_4	$\beta > 0$	If $0 < \beta < 1$: SPR3; if $\beta > 1$: Maxima	$E_4 = 1 + 2\beta$
P_5	$\beta < 1$	Maxima	$E_5 = (2 + \beta^2)$
P_6	$0 < \beta < 2$	SPR1	$E_6 = -(2 + \beta^2)/2$

Appendix A: Stability, existence and bifurcations of the equilibrium points

Here, we discuss the existence, stability and energy of the equilibria of the systems formed by two dipoles in an external electric field. These equilibria are summarized in Table I. We also analyze the bifurcations appearing between these equilibria as the electric field strength is increased.

1. Stability and existence of the equilibria for $\beta = 0$

For zero electric field, $\beta = 0$, the only isolated equilibria are P_1 and P_5 . Their nature is deduced by applying the method of Lagrange multipliers to the potential energy surface $\mathcal{V}_1(\mathbf{l}_1, \mathbf{l}_2, t = 0)$ Eq. (6) with $\beta = 0$, imposing the constraints $\{\mathbf{l}_i = (x_i, y_i, z_i) \mid |\mathbf{l}_i|^2 = 1\}_{i=1}^2$. There exist the two stable equilibria P_1 with minimal energy $E_1 = -2$, which are minima, and the two unstable equilibria P_5 with maximal energy $E_5 = 2$, which are maxima.

2. Stability and existence of the equilibria for $\beta \neq 0$ and $t \geq t_1$

For the general case $\beta \neq 0$, instead of using Cartesian variables, the analysis of the stability of the equilibria is carried out in spherical variables $\{(\theta_i, P_{\theta_i}), (\phi_i, P_{\phi_i})\}_{i=1}^2$. The equilibrium points of the Hamiltonian flux (9) for $t \geq t_1$ are the critical points of the potential \mathcal{V}_2 [see Eq. (8)],

$$\begin{aligned} \mathcal{V}_2(\theta_1, \phi_1, \theta_2, \phi_2, t \geq t_1) = & -\beta(\sin \theta_1 \sin \phi_1 + \sin \theta_2 \sin \phi_2) \\ & + [\sin \theta_1 \sin \theta_2 \cos(\phi_1 - \phi_2) - 2 \cos \theta_1 \cos \theta_2], \end{aligned}$$

together with the conditions $P_{\theta_i} = P_{\phi_i} = 0$. Obviously, the potential $\mathcal{V}_2(\theta_1, \phi_1, \theta_2, \phi_2, t \geq t_1)$ presents the same critical points as $\mathcal{V}_1(\mathbf{l}_1, \mathbf{l}_2)$ in Eq. (13). Thence, after expressing in spherical coordinates the (isolated) critical points $\{P_i\}_{i=1}^6$ detailed in Sec. II C, their stability can be inferred from the nature of the corresponding eigenvalues of the Hessian matrix associated to $\mathcal{V}_2(\theta_1, \phi_1, \theta_2, \phi_2, t \geq t_1)$.

a. The equilibria P_1

For the two equilibria P_1 , the eigenvalues of the Hessian matrix are:

$$(\beta^2/9, \beta^2/3, (9 - \beta^2)/3, (\beta^2 + 3)/3).$$

Because the equilibria P_1 only exist when $0 < \beta < 3$, its four eigenvalues are positive, which indicate that P_1 are minima. In other words, when they exist, equilibria P_1 are stable.

b. The equilibria P_2

The eigenvalues of the Hessian matrix of the two equilibria P_2 are:

$$\left(1 - \sqrt{\beta^2 + 1}, 1 + \sqrt{\beta^2 + 1}, 1 - \sqrt{\beta^2 + 4}, 1 + \sqrt{\beta^2 + 4}\right).$$

These eigenvalues indicate that P_2 are always rank-two saddle points because they have two positive and two negative eigenvalues. Then, equilibria P_2 are always unstable.

c. The equilibrium P_3

The eigenvalues of the Hessian matrix of the equilibrium P_3 are:

$$(\beta, \beta + 1, \beta - 3, \beta - 2).$$

The first and second eigenvalues are always positive. For $0 < \beta < 2$, the equilibrium P_3 is a rank-two saddle point because it has two positive and two negative eigenvalues. In the interval $2 < \beta < 3$, P_3 is a unstable rank-one saddle point (the third eigenvalue is positive). For $\beta > 3$, all the eigenvalues are positive, e.g., the equilibrium P_3 is a (stable) minimum.

d. The equilibrium P_4

The eigenvalues of the Hessian matrix of the equilibrium P_4 are:

$$(-\beta - 2, -\beta, -\beta - 3, 1 - \beta).$$

The first, second and third eigenvalues are always negative, while the fourth one changes from positive to negative for $\beta > 1$. Then, P_4 is an unstable rank-three saddle point when $0 < \beta < 1$, and a (unstable) maximum for $\beta > 1$.

e. The equilibria P_5

The eigenvalues of the Hessian matrix of the two equilibria P_5 are:

$$(-3\beta^2, -\beta^2, -\beta^2 - 3, \beta^2 - 1).$$

Because equilibria P_5 only exist for $\beta < 1$, all the eigenvalues are negative, such that P_5 are always (unstable) maxima.

f. The equilibria P_6

The eigenvalues of the Hessian matrix of the two equilibria P_6 are:

$$(\beta^2/2, 3, -1, (-\beta^2 + 4)/2).$$

The first and second eigenvalues are positive, the third one is negative and the fourth one is positive for $0 < \beta < 2$. Because equilibria P_6 only exist for $0 < \beta < 2$, they are unstable rank-one saddle points.

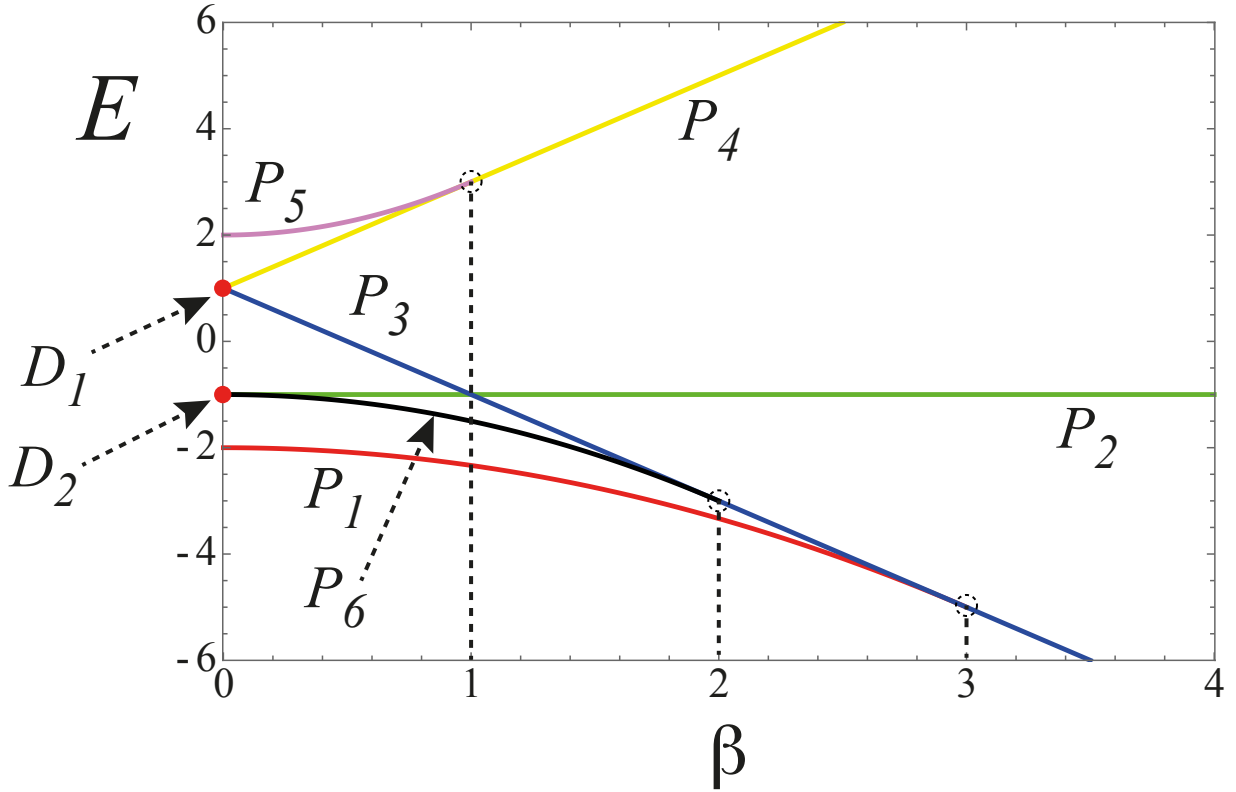


FIG. 10. Evolution of the energies of the critical points of $\mathcal{V}_1(\mathbf{l}_1, \mathbf{l}_2)$ in Eq. (13) as a function of the field parameter β . Dashed vertical lines and circles indicate the values of β where bifurcations occur.

3. Bifurcations

The bifurcations between the critical points are presented in Fig. 10 by the evolution of the equilibria energies as a function of the electric field parameter β . For the field-free case $\beta = 0$, besides the (isolated) equilibria P_1 and P_5 , which are respectively the *head-tail* ground state (minimum) configurations and the *head-head* and *tail-tail* maxima, the system presents the aforementioned two circles $D_{1,2}$ of degenerate equilibria, see Sec. II C. For $\beta > 0$, the circles of equilibria blow-up, and from D_1 and D_2 emerge the two isolated equilibria $P_{3,4}$ and $P_{2,6}$, respectively. In the interval $0 < \beta < 1$, the study of the stability of the equilibria shows that P_1 and P_5 are the absolute minima and maxima of the system, see Fig. 10, while $P_{2,3,4,6}$ are saddle points of rank-one, rank-two, rank-three and rank-one, respectively. As β increases towards $\beta = 1$, the equilibria P_4 and P_5 approach each other see Fig. 10, such that, at $\beta = 1$, a first Pitchfork bifurcation takes place: the two equilibria collide and only

the equilibrium P_4 survives afterwards, becoming the equilibrium of maximal energy. This is the expected configuration of maximal energy where both dipoles are located along the negative z_1 and z_2 axes, i. e., oriented antiparallel to electric field direction.

In the interval $0 < \beta < 3$, the equilibria $P_{1,3,6}$ approach each other (see Fig. 10), and at $\beta = 2$, equilibria P_3 and P_6 coincide. From this second pitchfork bifurcation, only equilibrium P_3 survives, becoming a saddle point of rank-one. Finally, at $\beta = 3$, a third Pitchfork bifurcation between the equilibria P_1 and P_3 occurs such that, for $\beta > 3$, only P_3 survives becoming the equilibrium of minimal energy. In this configuration of minimal energy, both dipoles are oriented along the field, i. e., along the positive $z_{1,2}$ axes. By further increasing β , $\beta > 3$, the dynamics is gradually dominated by the interaction with the electric field, and the landscape of the potential energy surface $\mathcal{V}_1(\mathbf{l}_1, \mathbf{l}_2)$ resembles the one obtained by neglecting the dipole-dipole interaction.

-
- [1] T. Lahaye, C. Menotti, L. Santos, M. Lewenstein, and T. Pfau, Rep. Prog. Phys. **72**, 126401 (2009).
 - [2] M. Schmitt, M. Wenzel, F. Böttcher, I. Ferrier-Barbut, and T. Pfau, Nature **539**, 259262 (2016).
 - [3] L. Chomaz, S. Baier, D. Petter, M. J. Mark, F. Wächtler, L. Santos, and F. Ferlaino, Phys. Rev. X **6**, 041039 (2016).
 - [4] I. Ferrier-Barbut, H. Kadau, M. Schmitt, M. Wenzel, and T. Pfau, Phys. Rev. Lett. **116**, 215301 (2016).
 - [5] B. Naylor, M. Brewczyk, M. Gajda, O. Gorceix, E. Maréchal, L. Vernac, and B. Laburthe-Tolra, Phys. Rev. Lett. **117**, 185302 (2016).
 - [6] S. Lepoutre, J. Schachenmayer, L. Gabardos, B. Zhu, B. Naylor, E. Marchal, O. Gorceix, A. M. Rey, L. Vernac, and B. Laburthe-Tolra, Nature Communications **10**, 1714 (2019)
 - [7] K.-K. Ni, S. Ospelkaus, D. Wang, G. Quéméner, B. Neyenhuis, M. H. G. de Miranda, J. L. Bohn, J. Ye, and D. S. Jin, Nature **464**, 1324 (2010).
 - [8] M. H. G. et al. de Miranda, A. Chotia, B. Neyenhuis, D. Wang, G. Quém'ener, S. Ospelkaus, J. L. Bohn, J. Ye and D. S. Jin, Nature Phys. **7**, 502 (2011).
 - [9] B. Yan, St. A. Moses, B. Gadway, J. P. Covey, K. R. A. Hazzard, A. M. Rey, D. S. Jin and J.

- Ye, Nature **501**, 521 (2013) .
- [10] Y. Tang, W. Kao, K.-Y. Li, S. Seo, K. Mallayya, M. Rigol, S. Gopalakrishnan, and B. L. Lev, Phys. Rev. X **8**, 021030 (2018).
- [11] S. Woutersen and H. Bakker, Nature **402**, 507 (1999).
- [12] T.-Q. Nguyen, J. Wu, V. Doan, B. J. Schwartz, S. H. Tolbert, Science **288**, 652 (2000).
- [13] D. P. Fahey, T. J. Carroll, and M. W. Noel, Phys. Rev. A **91**, 062702 (2015).
- [14] K. Rustomji, M. Dubois, B. Kuhlmeiy, C. Martijn de Sterke, S. Enoch, R. Abdeddaim, and J. Wenger, Phys. Rev. X **9**, 011041 (2019).
- [15] S. W. de Leeuw, D. Solvaeson, M. A. Ratner, and J. Michl, J. Phys. Chem. B **102**, 3876 (1998).
- [16] E. Sim, M. A. Ratner, and S. W. de Leeuw, J. Phys. Chem. B **103**, 8663 (1999).
- [17] J. J. de Jonge, M. A. Ratner, S. W. de Leeuw, and R. O. Simonis, J. Phys. Chem. B **108**, 2666 (2004).
- [18] R. González-Férez, M. Iñarrea, J. P. Salas, and P. Schmelcher, Phys. Rev. E **95**, 012209 (2017).
- [19] A. Zampetaki, J. P. Salas, and P. Schmelcher, Phys. Rev. E **98**, 022202 (2018).
- [20] E. Estevez-Rams , D. Estevez-Moya, and B. Aragón-Fernández, Chaos **28**, 023110 (2018).
- [21] C. A. Arango, W. W. Kennerly, and G. S. Ezra. J. Chem. Phys. **122**, 184303 (2005).
- [22] C. A. Arango and G. Ezra, Int. J. Bifurcat. Chaos, **18**, 1127 (2008).
- [23] T. Lahaye, C. Menotti, L. Santos, M. Lewenstein and T. Pfau, Rep. Prog. Phys. **72**, 126401 (2009).
- [24] M. J. Norman, C. Chandre, T. Uzer, and P. Wang, Phys. Rev. A **91**, 023406 (2015).
- [25] C. M. Dion, A. Keller, O. Atabek and A. Bandrauk, Phys. Rev. A **59**, 1382 (1999).
- [26] S. Trippel, T. Mullins, N. L. M. Müller, J. S. Kienitz, J. J. Omiste, H. Stapelfeldt, R. González-Férez, and J. Küpper, Phys. Rev. A **89**, 051401 (2014).
- [27] Andersen H.C., J. Comput. Phy. **52**, 24, (1983). E. Hairer, G. Wanner, *Solving Ordinary Differential Equations. II. Stiff and Differential-Algebraic Problems* (Springer Ser. Comput. Math., Springer-Verlag, 1996).
- [28] C. Froeschlé, E. Lega and R. Gonczi, Celes. Mech. Dyn. Astr. **67**, 41 (1997).
- [29] C. Froeschlé and E. Lega, Celes. Mech. Dyn. Astr. **78**, 167 (2000).
- [30] M. Fouchard, E. Lega and C. Froeschlé, Celes. Mech. Dyn. Astr. **83**, 205 (2002).

- [31] Ch. Skokos, J. Phys. A: Math. Gen. **34**, 10029 (2001).
- [32] Ch. Skokos, Ch. Antonopoulos, T.C. Bountis, M.N. Vrahatis, J. Phys. A: Math. Gen. **37**, 6269 (2004).